Design of Terahertz Band 1-Bit Reconfigurable Intelligent Surface: applications and coding methodologies

Minyu Zhang, and Yevhen Yashchyshyn

Abstract-In the forthcoming 6G wireless communication networks, it is crucial to address the challenges of massive information capacity and ultra-high data transmission rate. Terahertz (THz) band communication emerges as a promising candidate to meet these demands. However, the natural physical characteristics of THz signals, including significant attenuation in transmission and limited diffraction capabilities, pose substantial limitations on their practical applications. In recent years, reconfigurable intelligent surfaces (RIS) have garnered significant interest due to their exceptional potential in manipulating electromagnetic (EM) waves. RIS is anticipated to mitigate the challenges associated with THz communication. In this research, we introduce a RIS design featuring 1-bit phase modulation operating within THz bands. The RIS units leverage PIN diodes to dynamically adjust the unit structure, enabling dynamic encoding of the RIS metasurface based on the on and off states of diodes. In this paper, three typical application scenarios, including beam scanning, beam convolution, and radar cross section (RCS) reduction, are listed. Coding methodologies including fractional coding, convolution, Golay-Rudin-Shapiro (GRS) coding, and Genetic Algorithm (GA) coding, are deployed, and simulation results illustrate the effectiveness. This study lays the groundwork for the practical deployment and coding strategies of RIS in the THz bands, thereby facilitating the integration of THz technology into the next generation of 6G communication systems.

Keywords—Terahertz (THz); Reconfigurable Intelligent Surface (RIS); coding metasurface; beam scanning; beam convolution; RCS reduction

I. INTRODUCTION

N the past few years, the demands for wireless data transmission remarkably increases with the explosive growth of the mobile devices and diverse applications. This growth has steered the evolution trend of modern communication systems towards higher data rates, expanded system capacity, and broader transmission bandwidth, necessitating a shift towards higher operating frequency bands. 5G is the first generation of mobile communication systems that incorporates the millimeter wave (mm-Wave) band, boasting bandwidths reaching hundreds of MHz and enabling Gbps-level data transmission capabilities. The forthcoming

This work was supported in part by a project 101086493 — TeraHertz HORIZON-MSCA-2021-SE-01 and by the Institute of Radioelectronics and Multimedia Technology of Warsaw University of Technology..

Authors are with Warsaw University of Technology, corresponding author: Yevhen Yashchyshyn (e-mail: yevhen.yashchyshyn@pw.edu.pl).

6G wireless communication systems are anticipated to extend into the terahertz (THz) band [1], typically 0.1 to 10 THz range [2], promising to support data rates in the Tbps-level with exceptionally low latency [3]. As a promising candidate for 6G technology, the development of THz communication technologies have attracted great research interest in recent years [4]-[6].

One of the primary challenges in THz communication is the substantial losses within transmission, which results in significant attenuation of the received signal, thereby impacting the data transmission efficiency [7]. Meanwhile, THz electromagnetic (EM) signals will produce considerable attenuation during reflection and diffraction processes, which diminishes the coverage area and, consequently, the practical THz utility scenarios [8]. In addition, the narrow beam characteristic of the THz frequency range presents a challenge in achieving precise beam control and tracking, adding further complexity to the deployment and operation of THz communication systems [9].

To overcome these issues, the Reconfigurable Intelligent Surface (RIS) can be deployed in THz communication systems. The typical definition of RIS is a 2D programmable surface, whose unit state can be independently controlled to adjust the amplitude and phase of EM waves. This capability allows for the manipulation of the radio propagation environment, such as reflection, refraction and absorption [10]. By integrating RISs into communication systems, we can transform the traditional wireless environment into one both intelligent and adaptable [10], thereby enhancing the performance of the wireless networks. Similar concepts include coding metasurfaces [11], [12], which achieves control of EM signals by encoding independent units. So far, there have been some RIS designs based on PIN diodes and varactor diodes [13]-[16], and there are also a lot of RIS-related optimization works [17], [18].

In the context of diverse RIS applications within the THz band, we can employ distinct RIS coding methodologies to fulfill specific RIS functions. For instance, to combat the pronounced attenuation that occurs in THz signal propagation, RIS can implement beamforming by coding techniques to improve the signal gain, which in turn enhances the overall system performance. In another scenario, RIS can manipulate the incident signal through specific encoding



patterns, effectively reducing the radar cross section (RCS) [19], which is crucial for applications where stealth and low detectability are desired.

In this paper, a 1-bit RIS operating in the THz band is proposed. Meanwhile, three typical RIS application scenarios are demonstrated, and the corresponding coding methodologies are given. The key research contributions and distinctive features of our work are listed as follows:

- 1) Design of the 1-Bit RIS in THz Bands. We design a 1-bit RIS that can be applied in the THz bands. Its unit cell is controlled by a single PIN diode, and its on/off states achieve a stable phase difference of 180° within the operating bandwidth.
- 2) Coding Methodologies for Various THz RIS Applications. We listed three typical RIS application cases, including beam scanning, beam convolution, and RCS reduction. For each scenario, we provide corresponding coding methodologies, including fractional coding, convolution coding, Golay-Rudin-Shapiro (GRS) coding, and Genetic Algorithm (GA) coding. The high consistency between the calculated and simulated results proves the correctness of our coding methodologies.
- 3) EM Simulation Results for Verification. In addition to the numerical results calculated according to the coding methodologies, we performed EM simulations of the corresponding encoded THz RIS, and the results were used for comparison and verification. We found that the calculated results of the encoding showed good consistency with the simulation ones.

The remainder of this paper is organized as follows. Section II describes the design of the proposed 1-bit RIS unit. Using this THz RIS, we describe three application scenarios, i.e., beam scanning, beam convolution, and RCS reduction, in Section III, IV, and V. respectively, where the corresponding coding methodologies are analyzed in detail as well. Finally, Section VI provides the conclusions

II. THZ RIS ARRAY WITH 1-BIT UNITS

A. RIS Unit Design

The configuration of the proposed THz 1-bit RIS unit is depicted in Fig. 1, where related dimensions of the RIS unit are listed. The top substrate is F4BM265 with $\varepsilon_r = 2.65$, $\tan \delta =$ 0.002. The PIN diode connecting the grounded "dipoles" on the top surface of the RIS unit selects various resonant modes. The PIN diode is turned on or off according to the DC bias voltage, resulting in a phase difference of 180° within the operating bandwidth, ranging from 118 GHz to 126 GHz. The MA4AGFCP910 in MACOM is deployed [20], which displays decent performance in the THz band. The equivalent circuit models for both on and off states are presented in Fig. 2. From Fig. 3(a) and (b), it is evident that within the operating bandwidth, the reflection losses of both on and off states in the RIS unit are lower than 2.5 dB, while the phase difference remains close to 180° ($\pm 20^{\circ}$). Behind the ground plane layer, the substrate is FR4 with $\varepsilon_r = 4.4$, and a dielectric loss of $\tan \delta = 0.02$. The DC feeding line placed at the back is

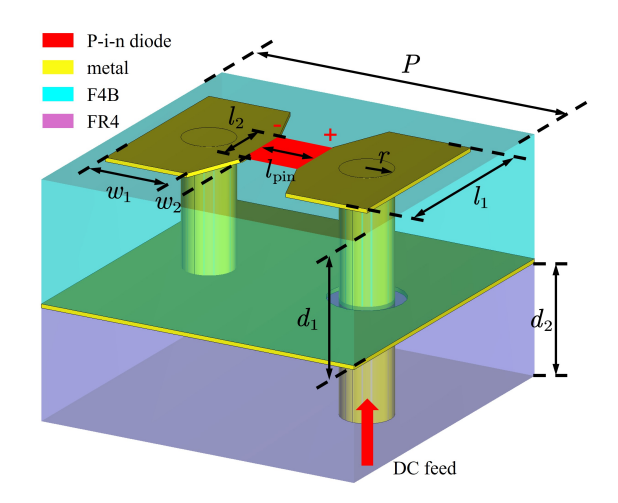


Fig. 1. Configuration of the 1-bit RIS unit, where P=1.5, r=0.1, $d_1=0.55$, $d_2=0.5$, $l_1=0.86$, $l_2=0.3$, $w_1=0.39$, $w_2=0.11$ (Unit: all in mm).

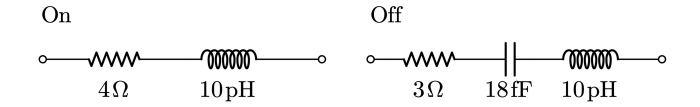


Fig. 2. Equivalent circuit models of the PIN diode MA4AGFCP910 in on or off states.

utilized to control the states of the diodes, and will not affect the RF response of the RIS unit.

B. RIS Array

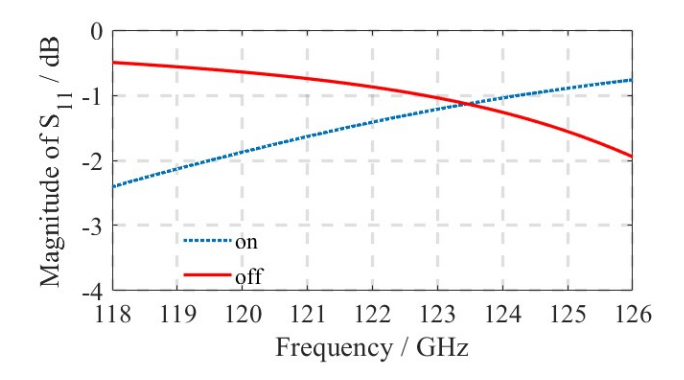
Based on the THz 1-bit RIS unit, the RIS array is demonstrated in Fig. 4, consisting of 256 unit cells (16×16). The total RIS array size is 24×24 mm², corresponding to 9.76×9.76 λ_0^2 , where λ_0 is the wavelength at the center frequency of 122 GHz.

Given that the two states of the RIS unit exhibit a phase difference of 180°, we can assign a 1-bit code to each RIS unit, where "0" represents the state where the PIN diode is turned off, and "1" signifies that the PIN diode is activated. Utilizing diverse RIS encoding strategies enables the achievement of various EM wave control objectives. A representative example is depicted on the right of Fig. 4.

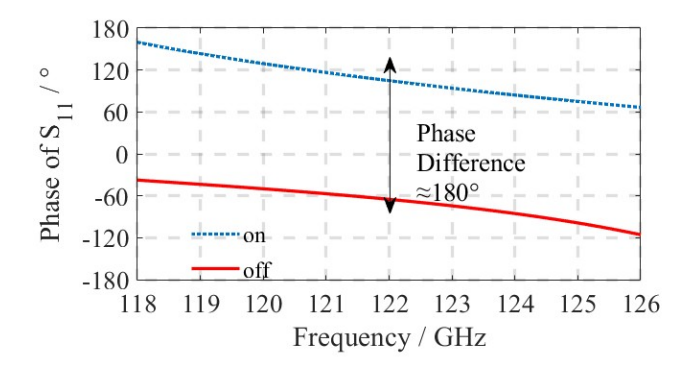
III. BEAM SCANNING

The first typical RIS application in the THz band is the beam scanning. Given the pronounced attenuation that characterizes THz band propagation and reflection, the ability to generate a high-gain THz beam with focused energy through RIS is crucial for both imaging and wireless communication. Concurrently, the high degree of reconfigurability in RIS facilitates the scanning of the reflected beam, significantly enhancing the scanning capabilities and coverage of THz signals.

However, employing traditional block coding to create phase gradients in RIS by the Generalized Snell's Laws [21] can



(a)



(b)

Fig. 3. (a) Magnitude response and (b) phase response of 2 states of the RIS unit.

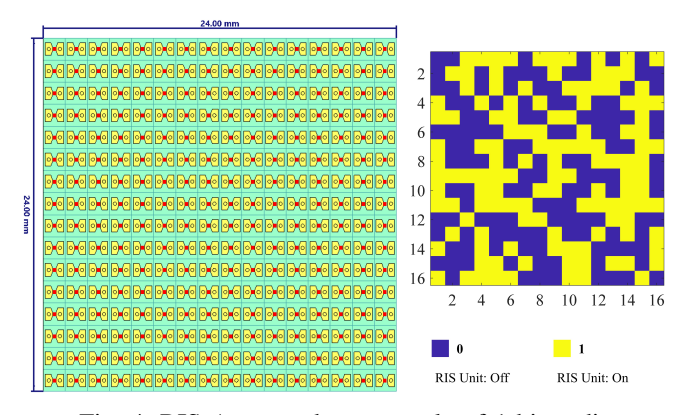


Fig. 4. RIS Array and an example of 1-bit coding.

substantially constrain the beam scanning range, particularly when the precision of RIS units is limited to a mere 1-bit. As illustrated in Fig. 5, with the 1-bit RIS array mentioned above, block coding with $N_x=1$ (periodic "1,0") and $N_x=3$ (periodic "1,1,1,0,0,0") results in a blind zone between the

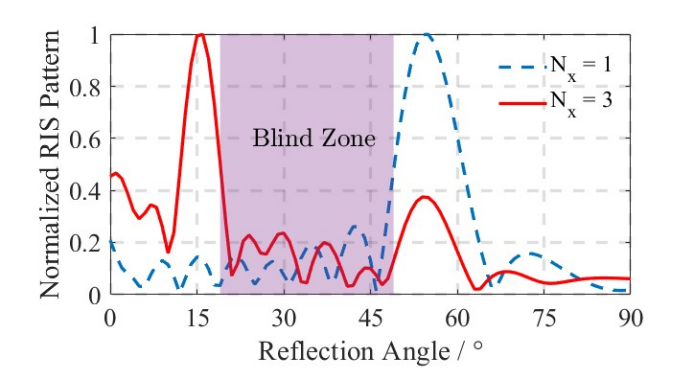


Fig. 5. Normalized reflection radiation patterns of RIS by block coding with $N_x = 1$ and $N_x = 3$, where there is a blind zone between 2 reflected beams (from 20° to 50°).

two reflected beams, from 20° to 50° , under normal incidence of the incident wave. This demonstrates that beam scanning achieved through block coding cannot encompass the entire space. Therefore, we employ fractional coding techniques [22] to enhance the flexibility of THz RIS beam scanning and to effectively address the scanning blind zone associated with block coding, ensuring comprehensive coverage of the scanning area.

A. Fractional Coding

In Fig. 6, the general methodology of the fractional coding under 1-bit condition is illustrated. In step 1, fractional code length is set as $N_x=1.25$, including periodic "0" and "1" bits. Next, we assign the fractional codes with length N_x to each RIS unit one by one. In step 3, two coding states in one RIS unit will be reset by selecting the major component as the final code sequence of RIS. More specifically, the determination of the second code bit can be taken as an example. From step 2, this bit can be interpreted as combinating "1" and "0" in a proportion of 25% to 75%, respectively, with "0" constituting the majority. Therefore, the resultant bit is" 0". It is noteworthy that when the weights of "0" and "1" within a RIS unit are equally balanced, selecting either "0" or "1" will have no obvious impact on the gradient variation of the RIS reflection phase.

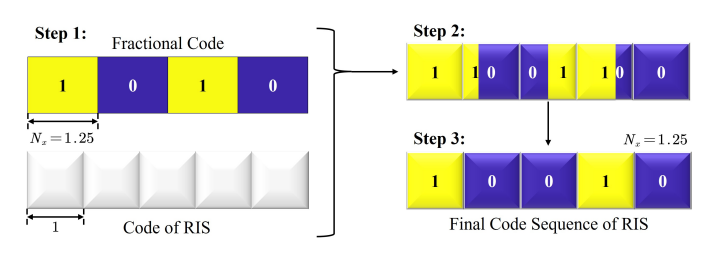


Fig. 6. Example of fractional coding methodology with $N_x = 1.25$.

TABLE I PERIODIC FRACTIONAL CODING SEQUENCE FOR THE THZ 1-BIT $16{\times}16$ RIS ARRAY

$\overline{N_x}$	Periodic Fractional Code Sequence	$\overline{\theta_r}$
1	$\cdots, 1, 0, \cdots$	±55°
1.1	$\cdots, 1, 0, 1, 0, 1, 1, 0, 1, 0, 1, 0, \cdots$	$\pm48^{\circ}$
1.25	$\cdots, 1, 0, 0, 1, 0, \cdots$	$\pm 39^{\circ}$
1.5	$\cdots, 1, 1, 0, \cdots$	$\pm 33^{\circ}$
1.75	$\cdots, 1, 1, 0, 0, 1, 0, 0, \cdots$	$\pm 27^{\circ}$
2	$\cdots, 1, 1, 0, 0, \cdots$	$\pm 24^{\circ}$
2.5	$\cdots, 1, 1, 1, 0, 0, \cdots$	$\pm 19^{\circ}$
3	$\cdots, 1, 1, 1, 0, 0, 0, \cdots$	$\pm 15^{\circ}$

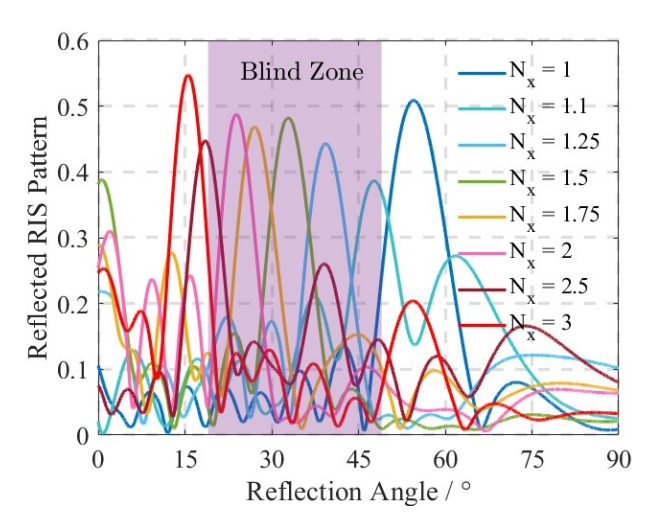


Fig. 7. Cover the previous blind zone in Fig. 5 by eight fractional coding sequences given in Table I.

To provide a general formula for the fractional coding, a filling factor q is introduced to refer to the proportion of the second bit in the combined RIS unit, where the i-th bit can be represented as:

$$q(i) = i - N_x \cdot \left[\frac{i}{N_x}\right],\tag{1}$$

where $[\cdot]$ is the rounding function. Therefore, the RIS unit sequence by fractional coding can be derived by:

$$C\left(i\right) = \begin{cases} \left\{ \left(\left[\frac{i}{N_x}\right] - 1 \right) / \frac{2\pi}{\mathsf{d}\varphi} \right\} / \frac{\mathsf{d}\varphi}{2\pi}, \ q\left(i\right) < 0.5 \\ \left[\frac{i}{N_x}\right] / \frac{2\pi}{\mathsf{d}\varphi} \right\} / \frac{\mathsf{d}\varphi}{2\pi}, \ q\left(i\right) \ge 0.5 \end{cases}$$
 (2)

where $\mathrm{d}\varphi=\pi$ since the RIS unit is 1-bit. The fractional coding method has excellent scalability, which is still applicable when the phase shift capacity of RIS is improved to 2-bit or above. In fabricated RIS designs, each column (or row) of the 1-bit elements can still be independently controlled via phase shifters or switching diodes. By appropriately programming these switches to alternate between different states according to the specified fractional pattern, the same beam-steering or RCS reduction effects can be realized.

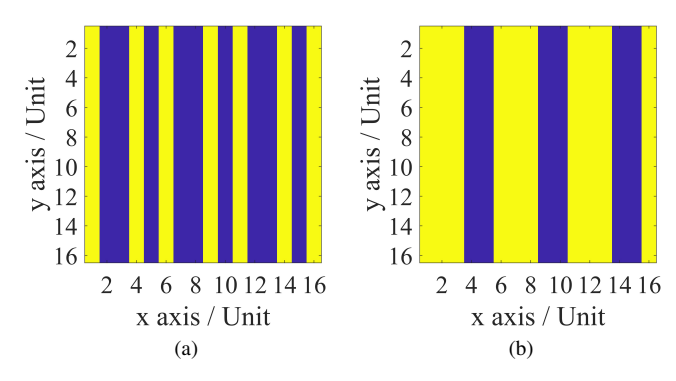


Fig. 8. RIS coding methods with (a) $N_x = 1.25$ and (b) $N_x = 2.5$, respectively.

B. Results

By gradually extending the code length N_x of the fractional coding, the proposed THz RIS in Section II is capable of performing beam scanning within a defined spatial range. As presented in Table I, we provide eight fractional coding sequences, each with distinct N_x values. With various code lengths, the coding cycle and the reflection angle of the RIS array to a normally incident EM wave differ accordingly. For instance, specific coding methods of the 16×16 array with $N_x=1.25$ and $N_x=2.5$ are provided in Fig. 8(a) and (b), respectively, where the periodic fractional code sequence in Table I can be found in the x gradient direction .

The normalized RIS reflection patterns for all fractional coding sequences listed in Table I are depicted in Fig. 7. For the 16×16 RIS array, fractional coding enables beam scanning from $\pm15^{\circ}$ to $\pm55^{\circ}$, with beam intervals of less than 10° . In contrast to block coding, 8 various fractional coding sequences with N_x values ranging between 1 and 3 are deployed, by which the RIS array is allowed to cover the blind zone illustrated in Fig. 5 with its reflected beams. In Fig. 7, within the blind zone, the main-lobe energy of fractional coding is lower than that of block coding because under fractional coding, the energy that should be concentrated in the main lobe is partially distributed to the side lobes, leading to a reduction in main-lobe amplitude. This issue can be mitigated by increasing the size of the RIS array or adopting an RIS with more accurate phase shifts (such as a 2-bit RIS).

IV. BEAM CONVOLUTION

In the preceding section, the fractional coding code length was denoted as N_x , indicating that the RIS reflection phase gradient change is confined to the x-axis direction. This limitation restricts beam scanning to a two-dimensional plane. To achieve free adjustment of the RIS reflection beam in three-dimensional space, it is necessary to incorporate the phase gradient changes along the y-axis as well. However, in three-dimensional space, the phase gradient change along the Y-axis should also be considered, introducing the fractional coding in both the x and y directions can lead to conflicts on the RIS array. To address this issue, an effective coding method, convolution coding [23], is deployed.

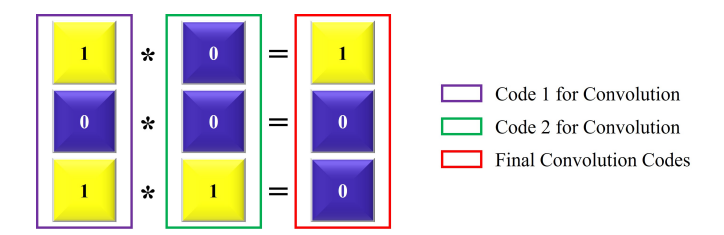


Fig. 9. Convolution coding methodology of 1-bit RIS.

A. Convolution Coding

The classic Fourier transform decomposes a time domain signal into its constituent frequency components. One of the important properties is the convolution theorem, which equates signal multiplication in the time domain to convolution in the frequency domain, which can be mathematically expressed as:

$$f(t) \cdot g(t) \stackrel{\text{FFT}}{\Leftrightarrow} f(\omega) * g(\omega).$$
 (3)

Meanwhile, the coding-pattern domain and the scatteringpattern domain can also be regarded as a pair of Fourier transforms [24]. Therefore the variables t and ω in formula (3) can be replaced with x_{λ} and $\sin \theta$, respectively, as:

$$f(x_{\lambda}) \cdot g(x_{\lambda}) \stackrel{\text{FFT}}{\Leftrightarrow} f(\sin \theta) * g(\sin \theta),$$
 (4)

where $x_{\lambda}=x/\lambda$ is the electrical length, and θ is the included angle to the norm.

Dating back to formula (3), g(w) is defined as the impulse function for simplification, thus:

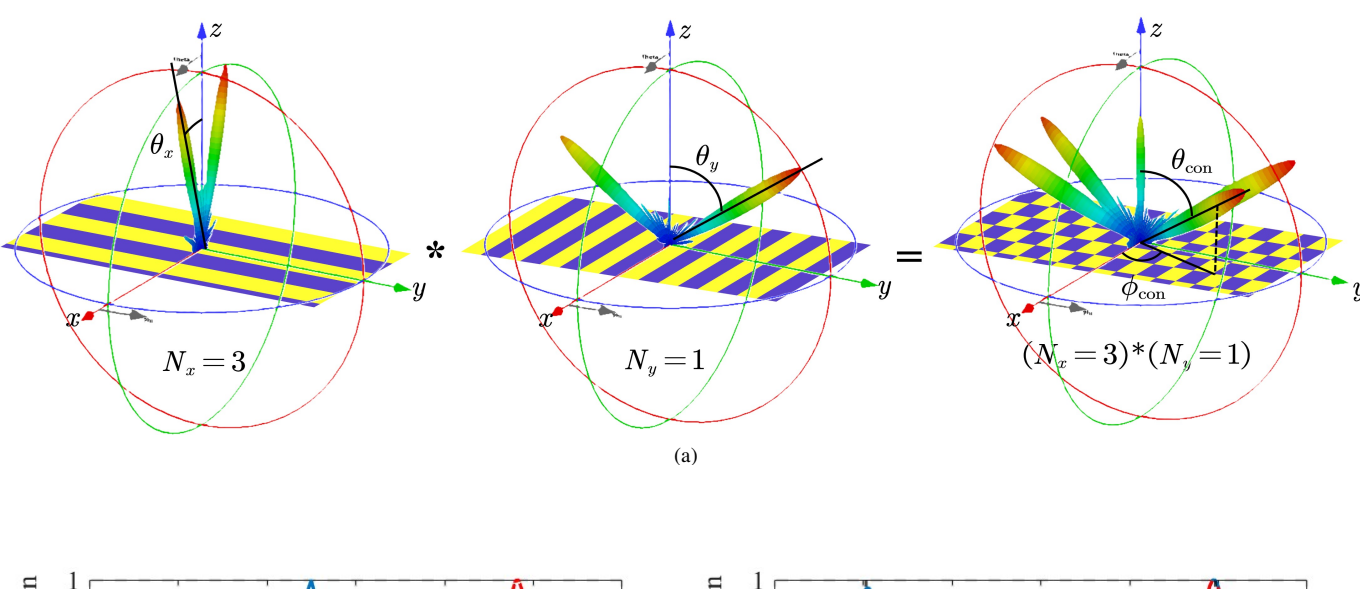
$$f(t) \cdot e^{j\omega_0 t} \stackrel{\text{FFT}}{\Leftrightarrow} f(\omega) * \delta(\omega - \omega_0) = f(\omega - \omega_0),$$
 (5)

which implies that the convolution of spectrum $f(\omega)$ with an impulse can be shifted by ω_0 without distortion. Similarly, substituting t and ω to expression (5), we can derive the principle of scattering-pattern shift, as:

$$E(x_{\lambda}) \cdot e^{jx_{\lambda}\sin\theta_{0}} \stackrel{\text{FFT}}{\Leftrightarrow} E(\sin\theta) * \delta(\sin\theta - \sin\theta_{0})$$

$$= E(\sin\theta - \sin\theta_{0}), \tag{6}$$

where the term $e^{jx_\lambda\sin\theta_0}$ depicts the electrical field distribution with phase gradient along a certain direction θ_0 . This phase gradient can be realized by the convolution coding



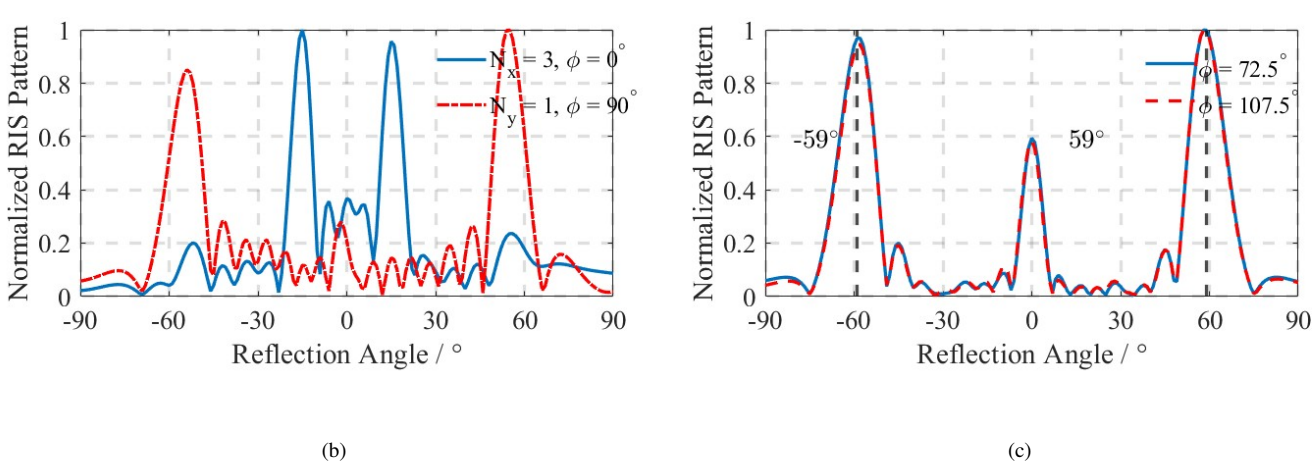


Fig. 10. (a) 3D simulated reflection patterns by convolution coding in THz 1-bit RIS. (b) Normalized reflection RIS patterns with independent fractional coding $N_x=3$ and $N_y=1$, respectively. (c) Normalized reflection RIS pattern with convolution coding calculated by 2 RIS codes in (b).

in RIS, i.e., we can deviate the scattering pattern $E(\sin \theta)$ from its original direction in angular coordinates by $\sin \theta_0$.

In summary, two independent RIS codes, such as the RIS code C_1 of the phase gradient in the x direction and C_2 in the y direction, can be convolved to achieve beam steering in 3D space. In our proposed 1-bit RIS, the methodology for implementing convolution coding is shown in Fig. 9, similar to the XOR operation.

B. Results

To verify the effectiveness of the convolution coding, this section employs two RIS coding schemes, $N_x=3$ and $N_y=1$, as illustrative examples. The RIS reflection beams for each of these individual codes are confined to the two-dimensional planes at $\phi=0^\circ$ and $\phi=90^\circ$, as depicted in Fig. 10(a). After convolving these two RIS codes, the angle of the resultant reflection beam in three-dimensional space can be determined as follows:

$$\begin{cases} \theta_{\text{con}} = \pm \sin^{-1} \left(\sqrt{\sin^2 \theta_x + \sin^2 \theta_y} \right) \\ \phi_{\text{con}} = \tan^{-1} \left(\left| \frac{\sin \theta_y}{\sin \theta_x} \right| \right) \text{ or } \pi - \tan^{-1} \left(\left| \frac{\sin \theta_y}{\sin \theta_x} \right| \right) \end{cases}$$
(7)

where θ_x and θ_y are the reflection angles of RIS code with $N_x=3$ and $N_y=1$, and $\theta_{\rm con},\phi_{\rm con}$ is the 3D reflection angle after convolution.

As depicted in Fig. 10(b), for RIS code with $N_x=3$, the reflection angle is $\theta_x=\pm 15^\circ, \phi_x=0^\circ$, while the reflection angle associated with the RIS code of $N_y=1$ is $\theta_y=\pm 55^\circ, \phi_y=90^\circ$. The above coded convolution and beamforming are calculated using formula (7), and the calculated result is $\theta_{\rm con}=\pm 59.2^\circ, \phi_{\rm con}=72.5^\circ$ or $107.5^\circ,$ illustrating that convolution coding can achieve beam shifting in the spatial domain. The EM simulation results are given in Fig. 10(c), where the peaks locate at $\pm 59^\circ$, agreeing well with the calculated ones. The simulation results validate the effectiveness of RIS convolution coding, showing its ability to dynamically expand the scanning range of the RIS reflected beam.

V. RCS REDUCTION

RCS is used to quantify the ability of a target to scatter an incident EM wave in a particular direction. The RIS unit neither absorbs nor dissipates the incident EM signals, instead, it reflects the incident energy in multiple directions, creating as many beams as possible. According to the law of energy conservation, the scattering energy of each individual beam will be significantly reduced, thus achieving an obvious decrease in RCS.

In this section, two RIS coding strategies are employed to accomplish RCS reduction. Initially, we utilize a non-repetitive binary coding in both the x and y directions, known as a Golay-Rudin-Shapiro (GRS) sequence [25], [26], to disperse the incident EM wave comprehensively. Subsequently, we introduce a GA coding based on the Internal Multiple-Port Method (IMPM) [27] to further minimize RCS. Upon comparison, this latter coding method demonstrates superior RCS reduction capabilities.

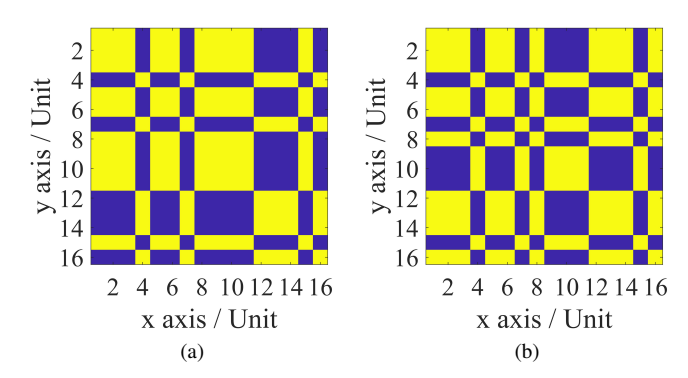


Fig. 11. GRS coding in (a) P-type and (b) Q-type for the 1-bit 16×16 RIS, respectively.

A. GRS Coding

Typically, there are two types of GRS coding, denoted as P-type and Q-type, which adhere to a recursive relationship between two interwoven sequences [26]. Both types exhibit analogous properties in terms of their gradient scattering effects. In this section, we focus on both types and make comparison on their performances.

The non-repetitive P-type GRS coding is produced through a straightforward deterministic process in two stages. Initially, an auxiliary binary sequence is crafted using the binary symbol set $\{-1,1\}$, as

$$\sigma_{P,0} = 1, \quad \sigma_{P,2n} = \sigma_{P,n}, \quad \sigma_{P,2n+1} = (-1)^n \sigma_{P,n}, \quad (8)$$

and the N-bit P-type GRS code can be mapped to $\{0,1\}$ by:

$$C_P(i) = \frac{1+\sigma_i}{2}, \text{ for } i = 1, 2, \dots, N.$$
 (9)

Taking the proposed 1-bit 16×16 THz RIS array as an instance, we can determine the P-type GRS coding sequence in x or y direction by applying formulas (8) and (9). The resulting 16-bit coding sequence is as follows:

$$C_P = \{1, 1, 1, 0, 1, 1, 0, 1, 1, 1, 1, 0, 0, 0, 1, 0\}.$$
 (10)

This P-type code is then deployed in both the x and y directions, whose resulting distribution of the final RIS unit states is depicted in Fig. 11(a).

The relationship between the P-type code and the Q-type GRS code is established in the auxiliary binary sequence:

$$\sigma_{Q,n} = \begin{cases} \sigma_{P,n}, & n = 0, 1, \dots, \frac{N}{2} - 1 \\ -\sigma_{P,n}, & n = \frac{N}{2}, \dots, N \end{cases}$$
(11)

Thus we are able to derive the expression for the corresponding 16-bit Q-type GRS code, as:

$$C_Q = \{1, 1, 1, 0, 1, 1, 0, 1, 0, 0, 0, 1, 1, 1, 0, 1\}.$$
 (12)

Similarly, the RIS unit distribution of the Q-type GRS code can be derived as given in Fig. 11(b).

The scattering RCS patterns of P-type and Q-type GRS codes at the center frequency of 122 GHz are provided in Fig. 12(a) and (b), respectively. Both codes achieve an RCS reduction of more than 16 dB, demonstrating good RCS

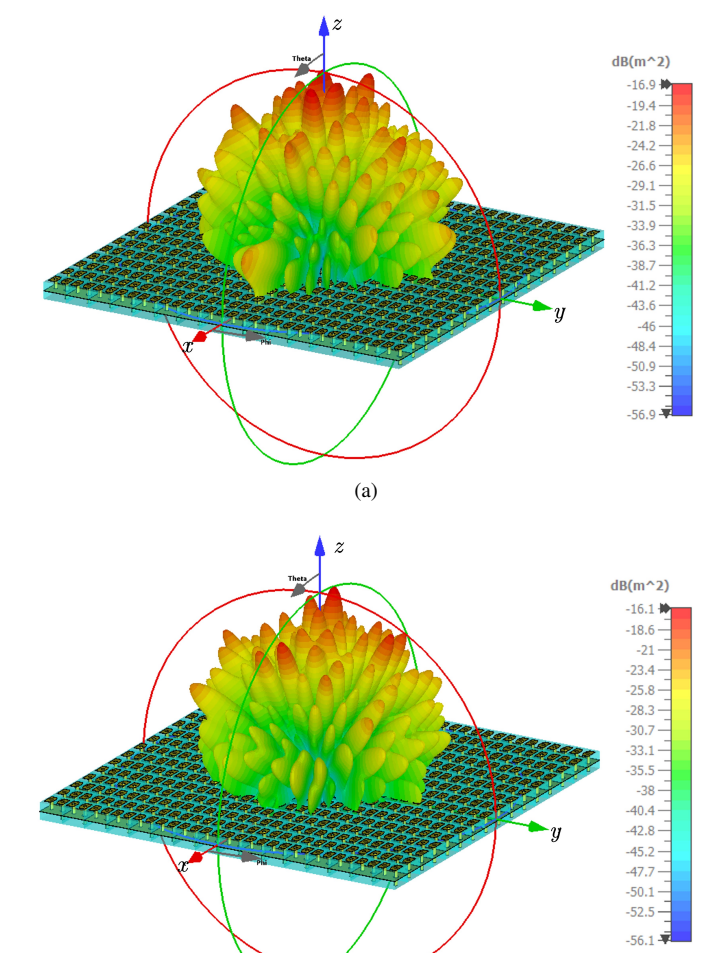


Fig. 12. RCS radiation patterns by RIS with (a) the P-type GRS code, and (b) the Q-type GRS code at the center frequency of 122 GHz.

(b)

reduction performance by GRS coding. Fig. 13 illustrates the RCS corresponding to the 16×16 RIS employing P- and Q-type GRS coding, and compares it with the RCS of the ground plane with equal size to the RIS. Within the THz operating bandwidth of the RIS, both P- and Q-type GRS coding exhibit comparable performance, and each achieves a substantial reduction in RCS relative to the ground plane.

B. GA Coding

From the last section, GRS coding can significantly reduce its RCS. However, as demonstrated in [26], GRS coding is not the most optimal approach for RCS reduction. To achieve even lower RCS, in this section, the Multiple Internal-Port Method (IMPM) [27] can be deployed to conduct detailed calculations on the proposed THz 1-bit RIS array. Subsequently, we utilize GA optimization to derive the most appropriate RIS coding, aiming to attain the minimum possible RCS. Compared with the GRS coding, the GA optimization generally exhibits stronger optimization capability but requires more computational resources and execution time. This is

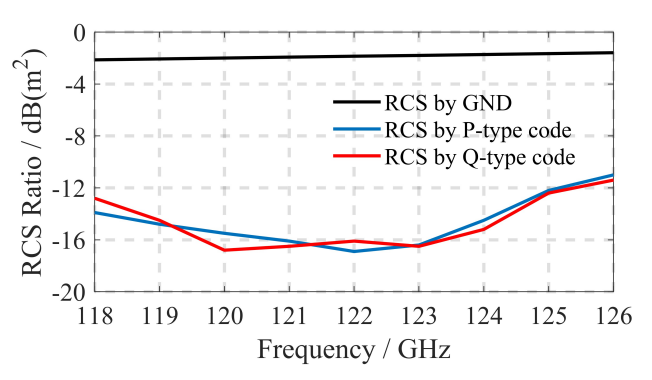


Fig. 13. Comparison of RCS reduction ratio across the THz operating bandwidth between P-type, Q-type coding and GND of the same size versus frequencies.

because it must evaluate and refine a large pool of candidate solutions over multiple generations, often within a very large search space.

In the proposed 16×16 1-bit RIS array, each RIS unit is equipped with a PIN diode. The array contains a total of M=256 PIN diodes, with the capability to switch each diode's state between on and off. A binary sequence $\mathbf{x}=[x_1,x_2,\cdots,x_M]^{\mathrm{T}}=\{0,1\}^M$ is utilized to illustrate the diode state. All M diodes can be considered as load impedance, and the m-th load can be either $Z_{\mathrm{L},m}=Z_{\mathrm{on}}$ with $x_m=1$ or $Z_{\mathrm{L},m}=Z_{\mathrm{off}}$ with $x_m=0$, whose value can be computed by circuits in Fig. 2. Then all these loads can be collected to form a diagonal load matrix $\mathbf{Z}_{\mathbf{L}}=\mathrm{diag}\{Z_{\mathrm{L},1},Z_{\mathrm{L},2},\cdots,Z_{\mathrm{L},M}\}$. In addition, the RIS array can be regarded as an M-port network, and $\mathbf{Z}\in\mathbb{C}^{M\times M}$ denotes the corresponding impedance matrix with one EM simulation.

Considering a plane incident wave to the RIS array, the voltage and current at the m-th internal port can be defined as v_m and i_m . Thus all voltages and currents can be collected into vectors, denoted as $\mathbf{v} = [v_1, v_2, \cdots, v_M]^T$ and $\mathbf{i} = [i_1, i_2, \cdots, i_M]^T$. According to the Thevenin Theorem, the voltage and current vectors can be related by:

$$\mathbf{v_{oc}} = \mathbf{v} - \mathbf{Zi},\tag{13}$$

where $\mathbf{v_{oc}} = [v_{\text{oc},1}, v_{\text{oc},2}, \cdots, v_{\text{oc},M}]^{\text{T}}$ shows the open-circuit voltages at all M internal ports. Considering the loads, the voltage and current vectors also satisfy:

$$\mathbf{v} = -\mathbf{Z}_{\mathbf{L}}\mathbf{i}.\tag{14}$$

Substitute (14) into (13), the current vector \mathbf{i} of all M RIS units can be calculated by [28]:

$$\mathbf{i} = -(\mathbf{Z} + \mathbf{Z}_{\mathbf{L}})^{-1} \mathbf{v}_{\mathbf{oc}}.\tag{15}$$

Based on the current vector, the total scattering pattern of the RIS array can be derived. Given the m-th port an excitation of 1 A while remaining all other ports open, the electric field excited by this port is $E_m(\Omega)$. All M electric fields can be collected into a matrix $\mathbf{E_{oc}} = [E_1, E_2, \cdots, E_M]$, and the total

TABLE II PARAMETERS IN THE GA OPTIMIZATION (17)

Parameter	Value			
Max. Generations	300			
Population Size	20000			
Cross Probability	0.8 (Uniformly Distributed)			
Mutation Probability	0.1 (Uniformly Distributed)			

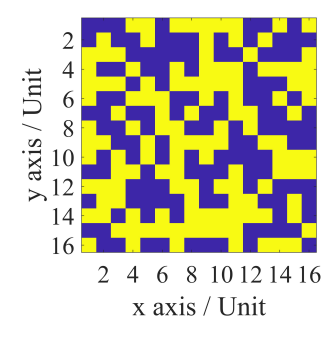


Fig. 14. Unit distribution of the proposed 16×16 RIS by GA coding.

scattering pattern by the RIS array can be written as:

$$E_s(\mathbf{\Omega}) = \sum_{m=1}^{M} i_m E_m(\mathbf{\Omega}) + E_{\text{oc}}(\mathbf{\Omega}) = \mathbf{E_{oc}} \mathbf{i} + E_{\text{oc}}(\mathbf{\Omega}), (16)$$

where $E_{\rm oc}(\Omega)$ is the scattering electric pattern with all M ports open.

To achieve the RIS coding x with the smallest RCS, the optimization problem can be formulated as:

$$\min_{\mathbf{x}} \max (|E_s(\mathbf{x}, \mathbf{\Omega})|)$$
s.t. $\mathbf{x} = \{0, 1\}^M$. (17)

which is a Boolean optimization problem that can be solved by heuristic algorithms such as GA. Related parameters for the GA optimization above are listed in Table II.

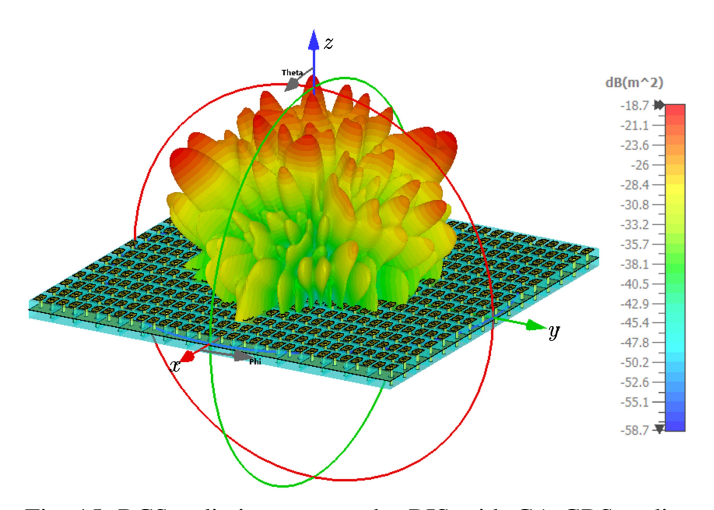


Fig. 15. RCS radiation patterns by RIS with GA GRS coding at the center frequency of 122 GHz.

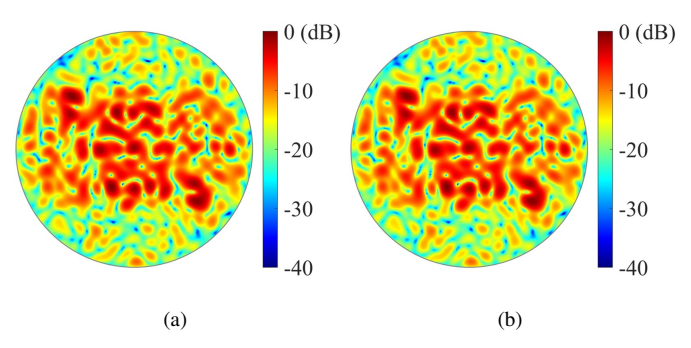


Fig. 16. Normalized (a) EM simulated and (b) the calculated radiation patterns by RIS with GA coding at the center frequency of 122 GHz.

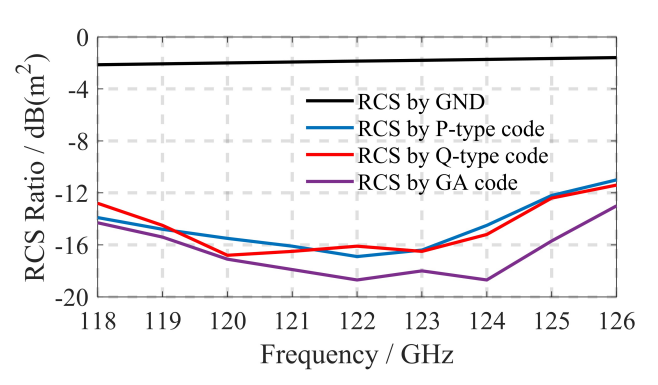


Fig. 17. Comparison of RCS reduction ratio across the THz operating bandwidth between P-type, Q-type coding, GA coding and GND of the same size versus frequencies.

Following optimization, the distribution of the RIS array units under the condition of minimal RCS is presented in Fig. 14. At the central frequency of 122 GHz, the scattering electric field of the RIS array is displayed in Fig. 15, achieving an RCS reduction ratio of 18.7 dB.

To verify the precision of our optimization approach, we compared the scattering pattern from CST EM simulations with the overall scattering pattern $E_s(\Omega)$ calculated using formula (16). The normalized outcomes are depicted in Fig. 16(a) and (b), respectively. It is evident that the electromagnetic simulation results closely match the calculated results, validating the accuracy of our optimization method.

In conclusion, we compared the RCS reduction ratios achieved by the two GRS codes and the GA codes across the given THz operating bandwidth. It can be observed that the proposed GA code outperforms the GRS by 1 to 2 dB throughout the entire bandwidth, indicating the superior performance of GA coding for RIS in RCS reduction.

C. Comparison With Relevant Works

To demonstrate the advantages of the proposed RIS, we compare it with other relevant reflection-based designs, as shown in Table III. Some existing RIS designs [28], [29], scattering methods rely on higher-order phase control (multibit phase shifts), which increases design complexity and

Reference	Phase type	Center frequency (GHz)	Bandwidth (GHz)	Number of units	Dimensions	Scanning range
[28]	4-bit	2.4	0.1	5×5	80 mm × 80 mm	$-50^{\circ} \sim +50^{\circ}$
[29]	2-bit	29	1	24×24	$5 \text{ mm} \times 5 \text{ mm}$	$+25^{\circ} \sim +65^{\circ}$
[30]	1-bit	28.5	2	20×20	$10 \text{ cm} \times 10 \text{ cm}$	$-60^{\circ} \sim +60^{\circ}$
This Work	1-bit	122	8	16×16	$24 \text{ mm} \times 24 \text{ mm}$	$\pm 15^{\circ} \sim \pm 55^{\circ}$

TABLE III
COMPARISONS BETWEEN THE PUBLISHED RIS WITH THIS WORK

hardware requirements. In contrast, our 1-bit RIS design utilizes simple phase control (180° phase shift), offering significant advantages in terms of cost-effectiveness, hardware implementation, and power consumption. Additionally, most studies focus on the sub-6 GHz or millimeter-wave bands [28]–[30], while our approach optimizes applications in the terahertz band (118 GHz to 126 GHz), specifically addressing the high attenuation and diffraction limitations in terahertz communication. Finally, our design integrates a variety of coding techniques, such as fractional coding and genetic algorithms, to achieve efficient beam control and performance optimization while reducing hardware dimensions.

VI. CONCLUSIONS

In this paper, we have designed a 1-bit RIS array operating in the THz band and investigated the corresponding coding strategies tailored to various RIS application scenarios, including beam scanning, beam convolution, and RCS reduction. The simulation outcomes indicate that the RIS array is capable of achieving relatively fine spatial beam scanning within the range of $\pm 15^{\circ}$ to $\pm 55^{\circ}$ through fractional coding. Furthermore, the RIS beam can be steered in the spatial domain by employing convolution coding with different coding sequences. Both GRS coding and GA optimization coding have demonstrated superior RCS reduction capabilities, with GA coding achieving an RCS reduction of over 16 dB within the frequency range of 119 GHz to 125 GHz. This research lays a technical foundation for the advancement of THz RIS and holds significant potential for future applications in the terahertz frequency domain.

REFERENCES

- [1] K. Rikkinen, P. Kyosti, M. E. Leinonen, M. Berg, and A. Parssinen, "Thz radio communication: Link budget analysis toward 6g," *IEEE Communications Magazine*, vol. 58, no. 11, pp. 22–27, 2020.
- [2] S. Dash, C. Psomas, I. Krikidis, I. F. Akyildiz, and A. Pitsillides, "Active control of thz waves in wireless environments using graphene-based ris," *IEEE Transactions on Antennas and Propagation*, vol. 70, no. 10, pp. 8785–8797, 2022.
- [3] H. Elayan, O. Amin, B. Shihada, R. M. Shubair, and M.-S. Alouini, "Terahertz band: The last piece of rf spectrum puzzle for communication systems," *IEEE Open Journal of the Communications Society*, vol. 1, pp. 1–32, 2020.
- [4] Z. Wan, Z. Gao, F. Gao, M. D. Renzo, and M.-S. Alouini, "Terahertz massive mimo with holographic reconfigurable intelligent surfaces," *IEEE Transactions on Communications*, vol. 69, no. 7, pp. 4732–4750, 2021
- [5] R. Su, L. Dai, and D. W. K. Ng, "Wideband precoding for ris-aided thz communications," *IEEE Transactions on Communications*, vol. 71, no. 6, pp. 3592–3604, 2023.

- [6] T. Do-Duy, A. Masaracchia, B. Canberk, L. D. Nguyen, and T. Q. Duong, "Throughput maximization in ris-assisted noma-thz communication network," *IEEE Open Journal of the Communications Society*, vol. 5, pp. 5706–5717, 2024.
- [7] T. Schneider, A. Wiatrek, S. Preussler, M. Grigat, and R.-P. Braun, "Link budget analysis for terahertz fixed wireless links," *IEEE Transactions on Terahertz Science and Technology*, vol. 2, no. 2, pp. 250–256, 2012.
- [8] A. A. A. Solyman and I. A. Elhaty, "Potential key challenges for terahertz communication systems," *International Journal of Electrical* and Computer Engineering (IJECE), 2021. [Online]. Available: https://api.semanticscholar.org/CorpusID:235590129
- [9] Q. Xue, C. Ji, S. Ma, J. Guo, Y. Xu, Q. Chen, and W. Zhang, "A survey of beam management for mmwave and thz communications towards 6g," *IEEE Communications Surveys and Tutorials*, vol. 26, no. 3, pp. 1520–1559, 2024.
- [10] M. Di Renzo, A. Zappone, M. Debbah, M.-S. Alouini, C. Yuen, J. de Rosny, and S. Tretyakov, "Smart radio environments empowered by reconfigurable intelligent surfaces: How it works, state of research, and the road ahead," *IEEE Journal on Selected Areas in Communications*, vol. 38, no. 11, pp. 2450–2525, 2020.
- [11] H. F. Ma and T. J. Cui, "Three-dimensional broadband ground-plane cloak made of metamaterials," *Nature Communications*, vol. 1, no. 1, p. 21, Jun 2010. [Online]. Available: https://doi.org/10.1038/ncomms1023
- [12] T. J. Cui, M. Q. Qi, X. Wan, J. Zhao, and Q. Cheng, "Coding metamaterials, digital metamaterials and programmable metamaterials," *Light: Science & Applications*, vol. 3, no. 10, pp. e218–e218, Oct 2014. [Online]. Available: https://doi.org/10.1038/lsa.2014.99
- [13] L. Dai, B. Wang, M. Wang, X. Yang, J. Tan, S. Bi, S. Xu, F. Yang, Z. Chen, M. D. Renzo, C.-B. Chae, and L. Hanzo, "Reconfigurable intelligent surface-based wireless communications: Antenna design, prototyping, and experimental results," *IEEE Access*, vol. 8, pp. 45913– 45923, 2020.
- [14] H. Sheng and Z. N. Chen, "Metasurface-loaded off-center monopoles with wideband radiation performance using characteristic mode analysis," *IEEE Transactions on Antennas and Propagation*, vol. 70, no. 11, pp. 10660–10668, 2022.
- [15] J. C. Liang, Q. Cheng, Y. Gao, C. Xiao, S. Gao, L. Zhang, S. Jin, and T. J. Cui, "An angle-insensitive 3-bit reconfigurable intelligent surface," *IEEE Transactions on Antennas and Propagation*, vol. 70, no. 10, pp. 8798–8808, 2022.
- [16] R. Wang, Y. Yang, B. Makki, and A. Shamim, "A wideband reconfigurable intelligent surface for 5g millimeter-wave applications," *IEEE Transactions on Antennas and Propagation*, vol. 72, no. 3, pp. 2399–2410, 2024.
- [17] K. Tekbiyik, G. K. Kurt, A. R. Ektı, and H. Yanikomeroglu, "Reconfigurable intelligent surfaces empowered thz communication in leo satellite networks," *IEEE Access*, vol. 10, pp. 121 957–121 969, 2022.
- [18] V. R. J. Velez, J. P. C. B. B. Pavia, N. M. B. Souto, P. J. A. Sebastião, and A. M. C. Correia, "Performance assessment of a ris-empowered post-5g/6g network operating at the mmwave/thz bands," *IEEE Access*, vol. 11, pp. 49 625–49 638, 2023.
- [19] Q. Zheng, W. Liu, Q. Zhao, L. Kong, Y.-H. Ren, and X.-X. Yang, "Broadband rcs reduction, antenna miniaturization, and bandwidth enhancement by combining reactive impedance surface and polarization conversion metasurface," *IEEE Transactions on Antennas and Propagation*, vol. 72, no. 9, pp. 7395–7400, 2024.
- [20] https://www.mouser.hk/datasheet/2/249/MA4AGP907_FCP910-838114. pdf, [Accessed 16-12-2024].
- [21] N. Yu, P. Genevet, M. A. Kats, F. Aieta, J.-P. Tetienne, F. Capasso, and Z. Gaburro, "Light propagation with phase discontinuities: Generalized laws of reflection and refraction," *Science*, vol. 334, no. 6054, pp.

- 333–337, 2011. [Online]. Available: https://www.science.org/doi/abs/10.1126/science.1210713
- [22] M. Yue, L. Liu, and X. Yuan, "Practical ris-aided coded systems: Joint precoding and passive beamforming," *IEEE Wireless Communications Letters*, vol. 10, no. 11, pp. 2345–2349, 2021.
- [23] S. Liu, T. jun Cui, L. Zhang, Q. Xu, Q. Wang, X. Wan, J. Gu, W. xuan Tang, M. Q. Qi, J. G. Han, W. L. Zhang, X. Y. Zhou, and Q. Cheng, "Convolution operations on coding metasurface to reach flexible and continuous controls of terahertz beams," *Advanced Science*, vol. 3, 2016. [Online]. Available: https://api.semanticscholar.org/CorpusID:18447112
- [Online]. Available: https://api.semanticscholar.org/CorpusID:18447112
 [24] C. Zhang, J. Yang, L. X. Yang, J. C. Ke, M. Z. Chen, W. K. Cao, M. Chen, Z. H. Wu, J. F. Chen, Q. Cheng, and T. J. Cui, "Convolution operations on time-domain digital coding metasurface for beam manipulations of harmonics," *Nanophotonics*, vol. 9, no. 9, pp. 2771–2781, 2020. [Online]. Available: https://doi.org/10.1515/nanoph-2019-0538
- [25] M. Moccia, C. Koral, G. P. Papari, S. Liu, L. Zhang, R. Y. Wu, G. Castaldi, T. J. Cui, V. Galdi, and A. Andreone, "Suboptimal coding metasurfaces for terahertz diffuse scattering," *Scientific Reports*, vol. 8, no. 1, p. 11908, Aug 2018. [Online]. Available: https://doi.org/10.1038/s41598-018-30375-z

- [26] M. Moccia, S. Liu, R. Wu, G. Castaldi, A. Andreone, T. Cui, and V. Galdi, "Coding metasurfaces for diffuse scattering: Scaling laws, bounds, and suboptimal design," *Advanced Optical Materials*, vol. 5, 07 2017.
- [27] S. Song and R. D. Murch, "An efficient approach for optimizing frequency reconfigurable pixel antennas using genetic algorithms," *IEEE Transactions on Antennas and Propagation*, vol. 62, no. 2, pp. 609–620, 2014.
- [28] J. Rao, Y. Zhang, S. Tang, Z. Li, S. Shen, C.-Y. Chiu, and R. Murch, "A novel reconfigurable intelligent surface for wide-angle passive beamforming," *IEEE Transactions on Microwave Theory and Techniques*, vol. 70, no. 12, pp. 5427–5439, 2022.
- [29] J. Jeong, J. H. Oh, S. Y. Lee, Y. Park, and S.-H. Wi, "An improved path-loss model for reconfigurable-intelligent-surface-aided wireless communications and experimental validation," *IEEE Access*, vol. 10, pp. 98 065–98 078, 2022.
- [30] J.-B. Gros, V. Popov, M. A. Odit, V. Lenets, and G. Lerosey, "A reconfigurable intelligent surface at mmwave based on a binary phase tunable metasurface," *IEEE Open Journal of the Communications* Society, vol. 2, pp. 1055–1064, 2021.